Accepted Manuscript

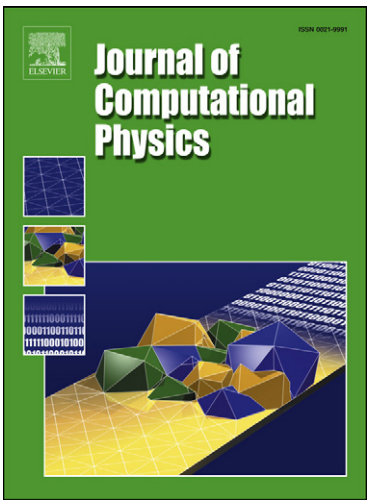

Linear dispersion-diffusion analysis and its application to under-resolved turbulence simulations using discontinuous Galerkin spectral/*hp* methods

R.C. Moura, S.J. Sherwin, J. Peiró

PII: S0021-9991(15)00417-9
DOI: http://dx.doi.org/10.1016/j.jcp.2015.06.020
Reference: YJCPH 5956

To appear in: *Journal of Computational Physics*

Received date: 24 December 2014
Revised date: 5 June 2015
Accepted date: 26 June 2015

Please cite this article in press as: R.C. Moura et al., Linear dispersion-diffusion analysis and its application to under-resolved turbulence simulations using discontinuous Galerkin spectral/*hp* methods, *J. Comput. Phys.* (2015), http://dx.doi.org/10.1016/j.jcp.2015.06.020

Linear dispersion-diffusion analysis and its application to under-resolved turbulence simulations using discontinuous Galerkin spectral/*hp* methods

R.C. Moura, S.J. Sherwin[1], J. Peiró

Aeronautics Department, Imperial College London, SW7 2AZ, United Kingdom

Abstract

We investigate the potential of linear dispersion-diffusion analysis in providing direct guidelines for turbulence simulations through the under-resolved DNS (sometimes called implicit LES) approach via spectral/*hp* methods. The discontinuous Galerkin (DG) formulation is assessed in particular as a representative of these methods. We revisit the eigensolutions technique as applied to linear advection and suggest a new perspective on the role of multiple numerical modes, peculiar to spectral/*hp* methods. From this new perspective, "secondary" eigenmodes are seen to replicate the propagation behaviour of a "primary" mode, so that DG's propagation characteristics can be obtained directly from the dispersion-diffusion curves of the primary mode. Numerical dissipation is then appraised from these primary eigencurves and its effect over poorly-resolved scales is quantified. Within this scenario, a simple criterion is proposed to estimate DG's effective resolution in terms of the largest wavenumber it can accurately resolve in a given *hp* approximation space, also allowing us to present points per wavelength estimates typically used in spectral and finite difference methods. Although strictly valid for linear advection, the devised criterion is tested against (1D) Burgers turbulence and found to predict with good accuracy the beginning of the dissipation range on the energy spectra of under-resolved simulations. The analysis of these test cases through the proposed methodology clarifies why and how the DG formulation can be used for under-resolved turbulence simulations without explicit subgrid-scale modelling. In particular, when dealing with communication limited hardware which forces one to consider the performance for a fixed number of degrees of freedom, the use of higher polynomial orders along with moderately coarser meshes is shown to be the best way to translate available degrees of freedom into resolution power.

Keywords: Under-resolved DNS, Implicit LES, Dispersion-diffusion analysis, Discontinuous Galerkin formulation, Spectral/*hp* methods

1. Introduction

Amongst a variety of existing methodologies for the simulation of turbulence, the under-resolved DNS (uDNS) approach has received increasing attention in recent years. In this approach, the goal is to resolve only the largest scales of motion, as in classical LES (Large Eddy Simulation), but no explicit modelling is used for the smallest scales. Accordingly, the unfiltered Navier-Stokes are simulated in a manner similar to DNS (Direct Numerical Simulation), except that an insufficient number of degrees of freedom is employed to resolve the flow and hence the use of the term under-resolved DNS. A distinction is also made between the uDNS strategy and the so-called implicit LES (iLES) approach [1]. In our interpretation, the term iLES is reserved for schemes where the numerical truncation has been demonstrated to implicitly mimic LES-like models. We note that for traditional low-order schemes, where the leading truncation error usually takes the form of a second-order diffusion operator, some kind of eddy-viscosity modelling can normally be recognized. On the other hand, we are adopting the uDNS expression for appropriately stabilized high-order methods since no direct correspondence between numerical errors and standard subgrid-scale (SGS) models is anticipated in this case.

Bypassing the need for explicit SGS models makes both iLES and uDNS approaches attractive since most of the theoretical and implementation complexities of traditional LES are avoided. It is argued that the former approaches

[1]Corresponding Author: s.sherwin@imperial.ac.uk

are also advantageous because, even if implicit turbulence models lack physics, the absence of modelling terms in the computations makes it possible to use a finer mesh than the one that would be used in classic LES for the same cost. As emphasized by Pope [2], LES models must be appraised not only by their physical accuracy, but also by their related computational cost, which together define a kind of effective performance for a given model. In a similar line of thought, Spalart points out that most works advocating sophisticated modelling "fail to show a clear advantage over the *same-cost* LES with a simplistic model" [3].

High-order spectral/*hp* methods [4] have been successfully used in under-resolved turbulence simulations with different discretizations, such as: the continuous Galerkin (CG) method [5, 6]; the discontinuous Galerkin (DG) formulation [7, 8]; the spectral difference (SD) method [9, 10]; as well as with the correction procedure via reconstruction (CPR) scheme [11, 12]. Apart from the CG discretization, where stability is usually enforced by added SVV (Spectral Vanishing Viscosity) [13], all these methods incorporate in their formulation some form of stabilization by means of upwind Riemann fluxes. It is recognized that these (either SVV or upwind fluxes) are the techniques responsible for providing dissipation at the under-resolved scales. We note that truncation error is also expected to contribute to the numerical dissipation. Other than that and regardless of the aforementioned ongoing applications, there is still little knowledge on *why* and *how* one can use spectral/*hp* methods for under-resolved turbulence simulations. The present study aims to clarify these issues by focusing on the discontinuous Galerkin formulation as a representative of high-order spectral/*hp* methods.

An early discussion on the suitability of DG for turbulence simulations was reported in [14, 15], where the scheme was found to successfully predict low-order statistics with fewer degrees of freedom (DOFs) than traditional numerical methods. More extensive assessments [16, 17] in the DNS of turbulent channel flows revealed that DG can predict high-order statistics with accuracy comparable to that of spectral methods for an equivalent number of DOFs. Regarding under-resolved simulations, a detailed study carried in [18] showed that, for a given number of DOFs, increasing the polynomial order is more effective than refining the mesh in order to improve the accuracy. This study considered discretizations up to 16th-order in the solution of the Taylor-Green vortex [19] test case and demonstrated that DG-based uDNS computations can outperform sophisticated LES methods in terms of accuracy (on a DOF basis) as long as the polynomial order is sufficiently high. This result was further confirmed by an extensive investigation reported in [8] where practical engineering test cases were considered. The effect of different types of mesh elements was assessed in [20] again through the Taylor-Green vortex problem and these were found to impact flow resolution mainly at small scales. This study however only considered discretizations up to 4th-order.

In the context of iLES, the modified equation analysis technique is usually employed [21] to justify why certain numerical schemes are particularly suited for implicit large eddy simulations. By resorting to Taylor series to rewrite discrete derivative expressions, modified equation analysis can reveal which PDE is actually governing a numerical solution. Due to the presence of truncation terms, the resulting PDE (referred to as the modified equation) differs from the physical PDE being discretized. In the analysis of low-order schemes for the discretization of the Navier-Stokes equations, a non-linear form of eddy-viscosity can sometimes be recognized in the first truncation terms [1].

An exploratory study on modified equation analysis for linear advection with DG was carried by the authors in [22]. Unfortunately, comparisons between modified equations and DG's dispersion-diffusion errors known from eigensolution analysis [23, 24] were not encouraging. We found that the representation of DG's numerical errors may not be satisfactory if just the first few truncation terms are taken into account. In some cases, up to ten truncation terms needed to be considered for an accurate representation. Moreover, the correspondence was verified to fail sometimes for the poorly-resolved wavenumbers, in which case truncation terms are not even representative of the numerical errors. Since these issues are unlikely to disappear for non-linear problems, a different approach is followed here.

In this work, DG's numerical errors are assessed directly through the eigensolution analysis, with particular focus on how numerical dissipation affects the under-resolved scales. While revisiting the eigensolutions technique, we discuss the role played by multiple numerical modes (peculiar to spectral/*hp* methods) and suggest a new perspective on the matter, from which "secondary" eigenmodes are seen to replicate the propagation behaviour of a "primary" mode. As a result, DG's propagation characteristics are obtained directly from the dispersion-diffusion curves of the primary mode. Then, from the primary diffusion eigencurves, a simple criteria (named 'the 1% rule') is proposed to estimate the effective resolution of the DG scheme for a given *hp* approximation space. More specifically, this rule estimates the maximum wavenumber that can be resolved accurately given the mesh spacing and polynomial order employed. Though strictly valid for linear advection, the proposed criteria is tested against one-dimensional Burgers turbulence and found to reliably predict the beginning of the dissipation range on turbulent energy spectra.

We highlight then the potential of linear dispersion-diffusion analysis in providing direct guidelines for the simulation of turbulence through the uDNS approach via spectral/*hp* methods.

This paper is organized as follows. The DG formulation for linear advection in one dimension is briefly summarized in Sec. 2. The eigensolution analysis technique is then revisited in Sec. 3, in which the role of secondary modes is discussed and where the 1% rule is introduced. In Sec. 4, this rule is tested against Burgers turbulence and the results are appraised in order to clarify *why* and *how* one can use spectral/*hp* methods (DG in particular) for turbulence simulations through the uDNS approach.

2. The semi-discrete DG formulation

Assuming suitable initial and boundary conditions are given, we consider the following scalar hyperbolic equation over the one-dimensional domain Ω:

$$\frac{\partial u}{\partial t} + \frac{\partial f}{\partial x} = 0 \,, \tag{1}$$

where $f = f(u)$ is the flux function, solely dependent on the solution $u = u(x,t)$. In the DG framework, the solution domain is divided among non-overlapping elements Ω_e such that $\Omega = \bigcup_e \Omega_e$. Within each of these elements, the solution is then approximated by a weighted sum of basis functions ϕ_j, namely

$$u|_{\Omega_e} \cong \sum_{j=0}^{P} c_j(t)\,\phi_j(\xi) \,, \tag{2}$$

where in this study ϕ_j is chosen to be the orthonormal Legendre polynomial of degree j, defined in the standard domain $\Omega_{st} = [-1,1]$, see [4, 25] for details. In order to obtain the coefficients c_j, the projection of Eq. (1) is required to vanish locally, i.e.

$$\int_{\Omega_e} \phi_i \left(\frac{\partial u}{\partial t} + \frac{\partial f}{\partial x} \right) dx = 0 \,, \quad \text{for } i \in \{0, \ldots, P\} \,. \tag{3}$$

Inserting Eq. (2) into Eq. (3) and given that the chosen basis functions are orthonormal, one can arrive at

$$\frac{h}{2}\frac{\partial c_i}{\partial t} = \int_{\Omega_{st}} \frac{\partial \phi_i}{\partial \xi} f \, d\xi - \int_{\Omega_{st}} \frac{\partial (\phi_i f)}{\partial \xi} \, d\xi \,, \tag{4}$$

where h is the size (length) of element Ω_e. Inter-element communication is allowed by the introduction of the numerical flux function, $\tilde{f}$, in the second integral on the right-hand side of Eq. (4) leading to

$$\frac{h}{2}\frac{\partial c_i}{\partial t} = \int_{\Omega_{st}} f\,\phi_i' \, d\xi - (\tilde{f}\phi_i)|_{\Omega_e^R} + (\tilde{f}\phi_i)|_{\Omega_e^L} \,, \tag{5}$$

where Ω_e^L and Ω_e^R denote the left and right boundaries of element Ω_e, respectively. The numerical flux $\tilde{f} = \tilde{f}(u_\ominus, u_\oplus)$ is a function of the values at the left ($u_\ominus$) and right ($u_\oplus$) sides of each interface considered. The full upwind flux is considered here, namely

$$\tilde{f}(u_\ominus, u_\oplus) = \frac{f(u_\ominus) + f(u_\oplus)}{2} + \left|\frac{\partial f}{\partial u}\right| \frac{u_\ominus - u_\oplus}{2} \,. \tag{6}$$

The dispersion-diffusion analysis performed in Sec. 3 will focus on the advection equation, namely Eq. (1) with $f = au$, where a is the constant advection speed. In this case, Eq. (5) becomes

$$\frac{h}{2a}\frac{\partial c_i}{\partial t} = \sum_{j=0}^{P} \mu_{ij} c_j - (\tilde{u}\phi_i)|_{\Omega_e^R} + (\tilde{u}\phi_i)|_{\Omega_e^L} \,, \tag{7}$$

where the constants μ_{ij} and the (normalized) numerical flux $\tilde{u} = \tilde{f}/a$ are given by

$$\mu_{ij} = \int_{\Omega_{st}} \phi_j \frac{\partial \phi_i}{\partial \xi} \, d\xi \quad \text{and} \quad \tilde{u}(u_\ominus, u_\oplus) = \frac{u_\ominus + u_\oplus}{2} + S_a \frac{u_\ominus - u_\oplus}{2} \,, \tag{8}$$

where $S_a = |a|/a$ is the sign of a. Using Eqs. (7–8) and assuming an equispaced mesh, the semi-discrete linear advection problem can be expressed in vector form for each mesh element as

$$\frac{h}{2a}\frac{\partial \vec{c}}{\partial t} = \boldsymbol{\mathcal{L}}\,\vec{c}_L + \boldsymbol{C}\,\vec{c} + \boldsymbol{\mathcal{R}}\,\vec{c}_R\,, \tag{9}$$

where $\vec{c} = \{c_0, \ldots, c_P\}^T$ and the indices L and R refer to the neighbour elements respectively at the left and right sides of the (central) element considered. The matrices in Eq. (9) are given by

$$\boldsymbol{C}_{i,j} = \mu_{ij} + \frac{1}{2}(1 - S_a)\,\phi_i(-1)\,\phi_j(-1) - \frac{1}{2}(1 + S_a)\,\phi_i(+1)\,\phi_j(+1)\,, \tag{10}$$

$$\boldsymbol{\mathcal{L}}_{i,j} = \frac{1}{2}(1 + S_a)\,\phi_i(-1)\,\phi_j(+1)\,,\quad \boldsymbol{\mathcal{R}}_{i,j} = -\frac{1}{2}(1 - S_a)\,\phi_i(+1)\,\phi_j(-1)\,. \tag{11}$$

3. Dispersion-diffusion analysis for DG

We apply the eigensolution analysis to the DG discretization of the linear advection equation to investigate the effect of numerical errors for under-resolved simulations. This technique has been applied for DG in different ways [23, 26, 24, 27, 28]. Here we follow the so-called temporal approach where a real wavenumber k is considered for the initial condition and a complex wave frequency w is assumed to govern the numerical solution.

When the analysis is applied to spectral/hp methods, several numerical modes are found in connection to each single (Fourier/Eigen) mode prescribed for the initial condition. As noted in [29], this fact is interpreted in different ways in the literature, but it is frequently assumed that only one numerical mode is important while all the others should be simply dismissed for being spurious. This question is also discussed in the present section and new perspective on the matter is offered, from which all the eigenmodes are seen to complement the propagation characteristics of a particular mode, here referred to as the primary one.

The fundamentals of eigensolution analysis for DG are reviewed in Sec. 3.1. Dispersion and diffusion curves are addressed in Sec. 3.2, where the role of multiple eigenmodes is discussed. Sec. 3.3 discusses the effect of numerical errors on the under-resolved scales and proposes a simple criterion to estimate the largest wavenumber that can be accurately resolved by a given hp setting.

3.1. Wave-like solutions and eigenmodes

Following the eigensolution analysis framework, one seeks for numerical solutions consistent with the analytic eigenfunctions of the linear advection equation in the form (hereafter, $i = \sqrt{-1}$)

$$u = \exp[i(kx - wt)]\,, \tag{12}$$

or, more specifically, solutions in which the element-wise approximating coefficients are related to the above wave-like solution through projection. Using orthonormal polynomials ϕ_j as basis functions, the coefficients associated to element Ω_e are given by

$$c_j(t) = \int_{\Omega_{st}} u\,(x_e + \xi h/2, t)\,\phi_j(\xi)\,d\xi\,, \tag{13}$$

where x_e denotes the centre of Ω_e. Hence, simple substitution yields

$$\vec{c}\,(t) = \vec{\alpha}\,\exp[i(kx_e - wt)]\,, \tag{14}$$

in which $\vec{\alpha} = \{\alpha_0, \ldots, \alpha_P\}^T$ and

$$\alpha_j = \int_{\Omega_{st}} \exp\,(ikh\xi/2)\,\phi_j(\xi)\,d\xi\,. \tag{15}$$

We stress that a single Fourier eigenmode can energize several numerical eigenmodes since there is no one-to-one correspondence between the employed polynomials and complex exponential functions which represent the eigenfunctions of the partial differential equation. Moreover, as discussed in Sec. 3.2, each of these numerical eigenmodes will behave as if related to different harmonics of the baseline wavenumber k of the original Fourier eigenmode.

It is worth noting that for orthonormal Legendre basis functions ϕ_j, one can analytically obtain $\alpha_j = \alpha_j(z)$, with $z = kh/2$, from the relations

$$\alpha_0 = \sqrt{2}\,\frac{\sin z}{z}\,,\;\; \alpha_1 = \frac{i\sqrt{6}}{z}\left(\frac{\sin z}{z} - \cos z\right)\,, \tag{16}$$

and, for $n \geq 1$,

$$\alpha_{n+1} = \frac{\sqrt{4n+6}}{z}\left[M_n \sin z + i\left(\frac{\sin z}{z} - \cos z\right)M_{n+1} + i\sum_{m=1}^{n}\sqrt{m+1/2}\,M_{m+n+1}\,\alpha_m\right]\,, \tag{17}$$

where $M_j = \mathrm{mod}(j,2)$ is the modulus of j after division by two.

In the temporal eigenanalysis, we use Eq. (14) with real k and complex w into the semi-discrete advection problem given in Eq. (9) to obtain

$$\frac{h}{2a}(-iw)\,\vec{c} = \left[\boldsymbol{\mathcal{L}}\,e^{-ikh} + \boldsymbol{\mathcal{C}} + \boldsymbol{\mathcal{R}}\,e^{+ikh}\right]\vec{c}\,, \tag{18}$$

which, by defining $\boldsymbol{\mathcal{M}} = 2\left[\boldsymbol{\mathcal{L}}e^{-ikh} + \boldsymbol{\mathcal{C}} + \boldsymbol{\mathcal{R}}e^{+ikh}\right]$, is equivalent to

$$-i\frac{wh}{a}\,\vec{\alpha} = \boldsymbol{\mathcal{M}}(kh)\,\vec{\alpha}\,. \tag{19}$$

This is clearly an eigenvalue problem (with $P+1$ solutions) of the discrete problem. The eigenvalue / eigenvector pairs $(\lambda_m, \vec{v}_m)$ are related to the variables in the discrete problem by

$$w_m = \frac{ia}{h}\lambda_m \;\text{ and }\; \vec{\alpha}_m \propto \vec{v}_m\,, \tag{20}$$

in which, without loss of generality, we define $\vec{\alpha}_m = \vec{v}_m/s_m$, being s_m the sum of the entries of $\vec{v}_m$. Hence, the general numerical solution (for element Ω_e) can be written as

$$\vec{c}\,(t) = \sum_{m=0}^{P} A_m\,\vec{v}_m\,\exp[i(kx_e - w_m t)] \tag{21}$$

or

$$c_j(t) = \sum_{m=0}^{P} A_m\,\boldsymbol{\mathcal{V}}_{j,m}\,\exp[i(kx_e - w_m t)]\,, \tag{22}$$

in which $\boldsymbol{\mathcal{V}} = \{\vec{v}_0, \ldots, \vec{v}_P\}$ and the constants A_m can be obtained from the initial condition. More specifically, when $u(x,0) = \exp(ikx)$ a simple projection yields

$$\sum_{m=0}^{P} A_m\,\vec{v}_m\,\exp(ikx_e) = \vec{\alpha}\,\exp(ikx_e)\,, \tag{23}$$

where Eqs. (14) and (21) were used with $t = 0$. Accordingly, $\vec{A} = \{A_0, \ldots, A_P\}^T$ is given by $\vec{A} = \boldsymbol{\mathcal{V}}^{-1}\vec{\alpha}$.

Using Eq. (22), the element-wise numerical solution within Ω_e reads

$$u_e(\xi,t) = \sum_{j=0}^{P} c_j(t)\,\phi_j(\xi) = \sum_{j=0}^{P}\sum_{m=0}^{P} A_m\,\boldsymbol{\mathcal{V}}_{j,m}\,\phi_j(\xi)\,\exp[i(kx_e - w_m t)]\,, \tag{24}$$

which can be rewritten as

$$u_e(\xi,t) = \sum_{m=0}^{P} A_m\,\sigma_m(\xi)\,\exp[i(kx_e - w_m t)] = \exp(ikx_e)\sum_{m=0}^{P} A_m\,\sigma_m(\xi)\,\exp(-iw_m t)\,, \tag{25}$$

where the element-wise eigenfunctions $\sigma_m(\xi)$ of the discrete problem were introduced, namely

$$\sigma_m(\xi) = \sum_{j=0}^{P} \boldsymbol{\mathcal{V}}_{j,m}\, \phi_j(\xi)\ . \tag{26}$$

Each σ_m can be interpreted as the transformation of the associated $\vec{v}_m$ into physical space. It should be understood from Eq. (25) that while the factor $\exp(ikx_e)$ accounts for wave-like variations from one element to another, the discrete eigenfunctions $\sigma_m(\xi)$ must account for wave-like variations *inside the elements*. The effect of the latter will be particularly significant in simulations with coarse meshes and high values of P.

In summary, Eqs. (21–25) indicate that the numerical solution is composed by $P+1$ modes which, through their respective values of w_m, propagate with different dispersion and diffusion characteristics. The eigenvalues λ_m of the discrete problem are related to these characteristics of the numerical approximation to the original advection problem and so are discussed in the next section.

3.2. Dispersion / diffusion curves and secondary modes

Following the exact dispersion relation for the linear advection equation, $w = ak$, it is possible to define a modified wavenumber k^* as the ratio between the (numerical) angular frequency and the advection speed. One modified wavenumber can therefore be obtained from each angular frequency w_m, such that $w_m = ak^*_m$. The natural interpretation is that each eigenmode (m) of the numerical solution will behave as if related to k^*_m instead of k. From Eq. (19), we note that $\boldsymbol{\mathcal{M}}$ is a function of k and so both w_m and k^*_m are also functions of the 'baseline' wavenumber k.

Employing the relation between w_m and λ_m given in Eq. (20) yields

$$\mathrm{Real}(k^*_m) = \frac{\mathrm{Real}(w_m)}{a} = -\frac{\mathrm{Imag}(\lambda_m)}{h}\ , \quad \mathrm{Imag}(k^*_m) = \frac{\mathrm{Imag}(w_m)}{a} = \frac{\mathrm{Real}(\lambda_m)}{h}\ . \tag{27}$$

For pure advection, deviations of $\mathrm{Real}(k^*)$ from k are related to dispersion (lead or lag phase errors) while deviations of $\mathrm{Imag}(k^*)$ from zero corresponds to diffusion (numerical dissipation), assuming $\mathrm{Imag}(k^*) < 0$.

The case $P = 2$ is considered in Fig. 1(a), where the real and imaginary parts of the modified wavenumbers k^*_m are displayed against the baseline wavenumber k, each curve corresponding to a different eigenmode (m). As usual, the axes are normalized by the number of degrees of freedom employed, $N_{\mathrm{dof}} \propto (P+1)/h$. We also note that in a spectral/hp discretization $h/(P+1)$ is representative of the smallest length scale that can be captured by the hp setting. The mode in the centre of these plots, i.e. the one that recovers $k^* = k$ as $k \to 0$, will be identified as the "primary" mode, while the remaining branches are simply called "secondary" modes. The role played by different numerical modes is discussed in what follows.

Since each $\overline{k^*_m} = k^*_m h/(P+1)$ is a periodic function of $\overline{k} = kh/(P+1)$, with period 2π, it is sufficient to analyse $\overline{k^*_m}$ for $-\pi \le \overline{k} \le \pi$, as shown in Fig. 1(a), which displays this periodicity for the real and imaginary parts of $\overline{k^*_m}$. All the eigencurves of secondary modes appearing in Fig. 1(a) are just replicas of the primary mode's eigencurve translated of $2\pi/(P+1)$ in the normalized $\overline{k}$-axis, both for dispersion and diffusion. This symmetry can easily be verified for higher values of P and happens to be true not only for the eigenvalues λ_m, but also for the eigenvectors $\vec{v}_m$. The eigenvectors' symmetry is illustrated in Fig. 1(b) for the eigenmatrix's entries $\boldsymbol{\mathcal{V}}_{1,m}$ again for the case $P = 2$.

After realising that the eigencurves of secondary modes are simply (equispaced) replicas of the primary mode's eigencurves, one can conclude that all the propagation properties of the secondary modes are essentially contained in the eigencurves of the primary mode. In fact, given $\overline{k}$, the eigenvalues and eigenvectors of the numerical solution can be found on the different $(P+1)$ eigencurves at a fixed value of $\overline{k}$ or, alternatively, on the values along the primary mode's eigencurves at the equivalent equispaced $(P+1)$ values of $\overline{k}$. Thanks to the symmetries, these equivalent values of $\overline{k}$ are simply replicas of the baseline $\overline{k}$ separated by $2\pi/(P+1)$ in the normalized $\overline{k}$-axis. Both ways of obtaining the eigenvalues are illustrated in Fig. 2(a) for $P = 2$ and $\overline{k} = \pi/6 \approx 0.52$. The procedure for the eigenvectors is similarly straightforward, but has to be performed in a component-wise manner.

The nature of the secondary modes can be interpreted as follows. If a single Fourier component is prescribed as initial condition through a projection, the hp discretization space will perceive it as a variety of polynomial components which will correspond to a series of numerical eigenfunctions, instead of just one. We note nevertheless that such representation corresponds to the optimal approximation (in the L^2 norm) provided that a Galerkin projection is used.

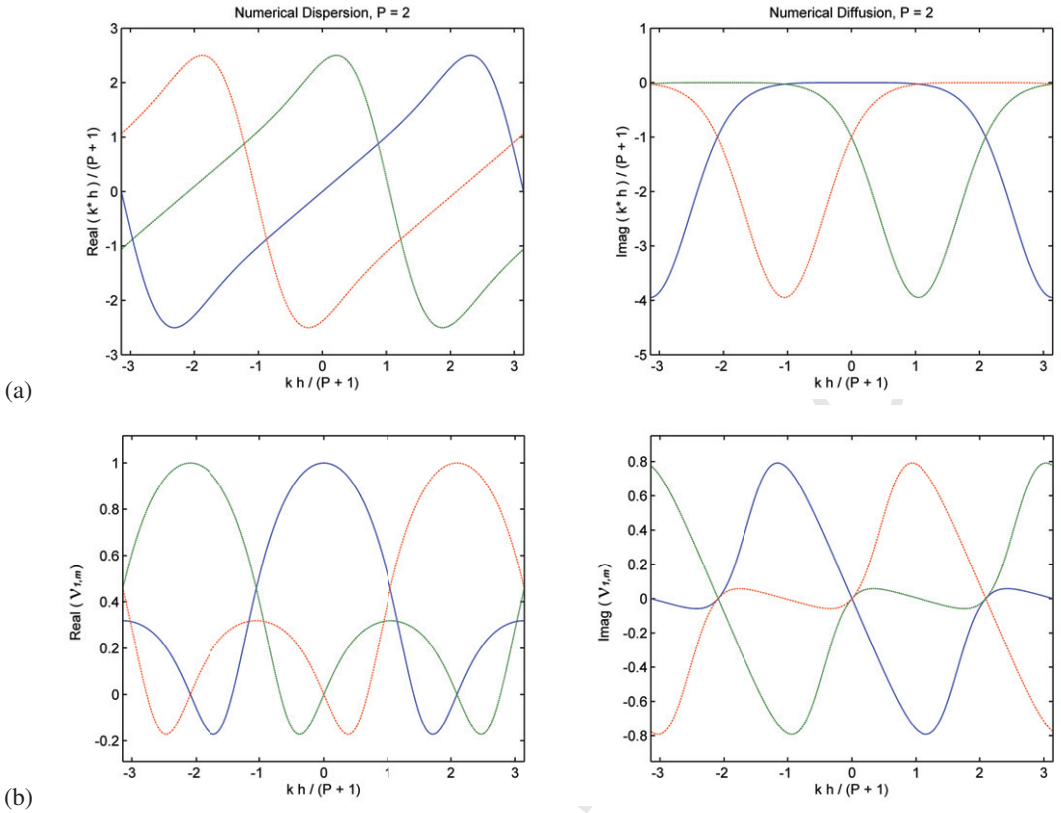

Figure 1: For a full upwind DG discretization with $P = 2$: (a) real (left) and imaginary (right) parts of the modified wavenumbers k_m^* vs. the baseline wavenumber k and (b) real (left) and imaginary (right) parts of an eigenmatrix's entries $\boldsymbol{\mathcal{V}}_{1,m}$ vs. the baseline wavenumber k.

The proposed interpretation is illustrated in Fig. 2(b), where we observe the approximation of $u(x, 0) = \cos(\pi x)$ using a $P = 2$ discretization with 8 equispaced elements in the interval $0 \leq x \leq 4$. The discrete approximation to the cosine function is decomposed into three numerical modes (ev_1, ev_2 and ev_3) such that, from Eq. (25),

$$ev_m(x, 0) = A_m \exp(ikx_e)\, \sigma_m(\xi)\,, \quad \text{for } m = 1, 2, 3, \tag{28}$$

where the values of A_m are indicated by the scale of the vertical axis of each numerical eigenmode in Fig. 2(b). The initial projection of $\cos(\pi x)$ leads to a primary contribution from ev_1 which corresponds to the primary mode and captures most of the cosine function. However, the two other numerical eigenmodes (ev_2 and ev_3) also contribute to the optimal approximation.

The DG scheme then propagates each of the discrete eigenmodes according to their own (apparent) wavenumbers as highlighted by the dotted lines between plots (a) and (b) in Fig. 2. These secondary modes represent "intrusive" wavenumbers that were not present in the initial condition, but that should not be considered unphysical or spurious as they are indeed improving the numerical approximation. We show below that secondary eigenmodes can work together via superposition to accurately propagate the initial projection. However, as they propagate forwards in time, the numerical diffusion also acts on the secondary modes.

In Fig. 2(c) the considered test case is shown at $t = 1/2$, after being advected a distance of one mesh element with a unit velocity. The solution still consists of three eigenmodes, but with reduced amplitudes since they were subjected to different amounts of dissipation during the propagation. The primary mode ev_1 has its eigenvalue within the linear regions of dispersion/diffusion curves and thus propagates without significant diffusion. Mode ev_2 has the smallest diffusion of the two secondary modes and so maintains some of its original shape, whereas ev_3 has a large numerical dissipation and by $t = 1/2$ has already decayed to a negligible amplitude.

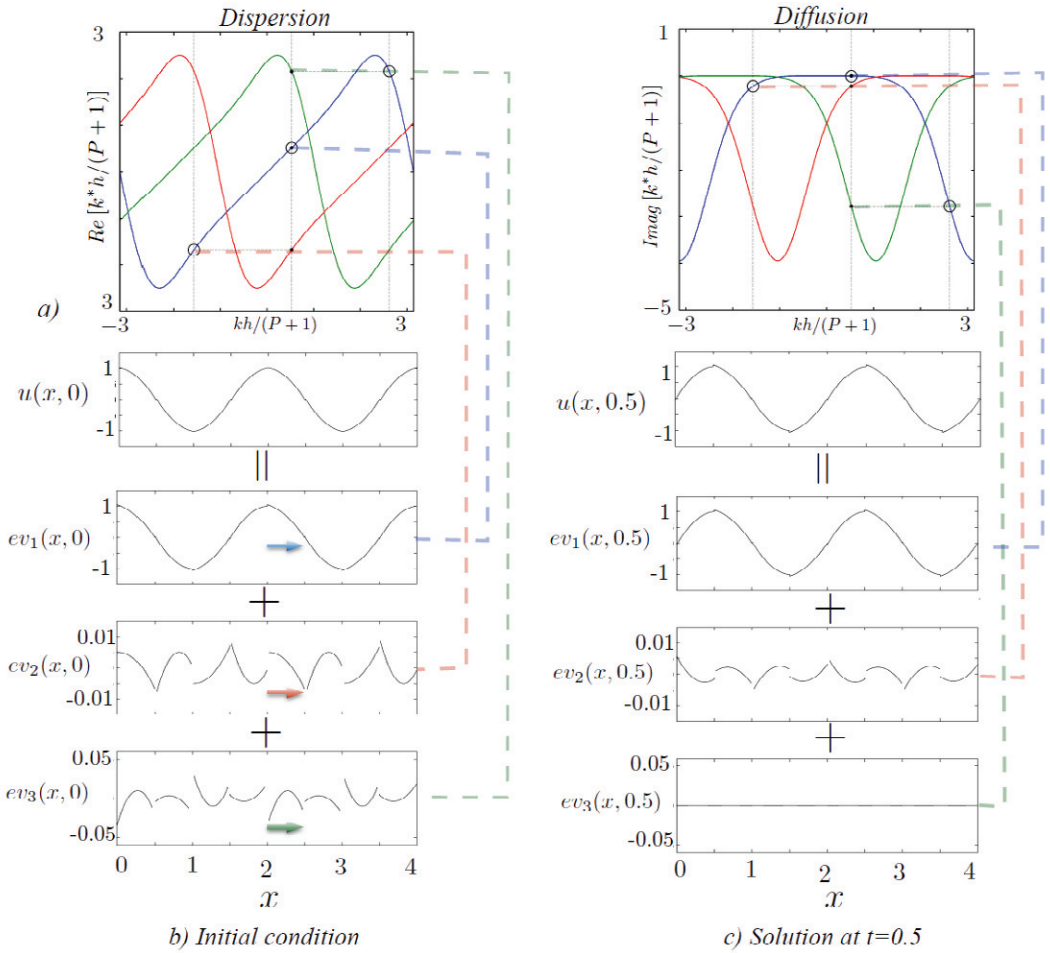

Figure 2: Understanding the primary and secondary eigenmodes. (a) For a fixed value of $kh/(P+1) = \pi/6 \approx 0.52$ we obtain three eigenvalues. Two secondary eigenvalues can be considered as replicas of the primary eigenvalue separated by $2\pi/(P+1) = 2\pi/3$. (b) A cosine wave initial condition is perceived through a Galerkin projection as a primary mode ev_1 and two secondary modes ev_2, ev_3. (c) All three eigenmodes contribute to the numerical advection of the initial condition but decay at different rates as defined by the imaginary part of their respective eigenvalues.

Fig. 3 illustrates the distribution of secondary modes when a higher value of P is considered. This figure represents an example with $P = 8$ again for $\bar{k} = \pi/6 \approx 0.52$. One can see that each secondary mode acts as the primary mode at a different $\bar{k}$. As in Fig. 2(a), the eigenvalues shown as circles are associated with values of $\bar{k}$ separated of $2\pi/(P+1)$ from each other. The primary eigenvalue, i.e. the one directly related to the baseline wavenumber $\bar{k}$, is shown as a solid circle. It is also worth noting that the primary solution mode is not necessarily the one subjected to the lowest dispersion/diffusion errors.

To further understand the role of the secondary modes we can consider the following analysis. Let $\mathbb{W}$ be the set of values of m whose associated modes (or whose apparent wavenumbers) lie on the linear regions of dispersion/diffusion curves. More precisely, for $m \in \mathbb{W}$, the relations

$$\overline{k_m^*} = \bar{k} + 2\pi q_m/(P+1) \;\text{ or }\; k_m^* h = kh + 2\pi q_m \tag{29}$$

are very good approximations, for some $q_m \in \mathbb{Z}$. A larger portion of the eigenmodes will follow the relations above as P increases, see Fig. 3 for example. These modes ($m \in \mathbb{W}$) clearly represent the well-resolved part of the numerical solution.

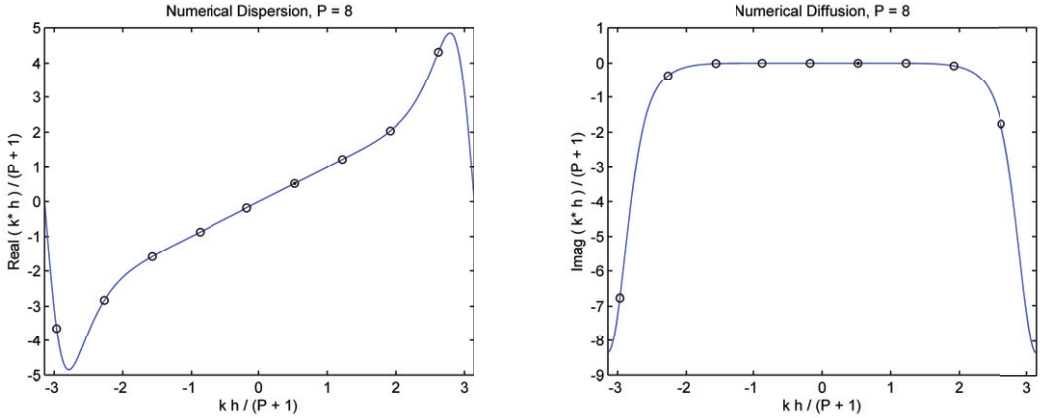

Figure 3: Real (left) and imaginary (right) parts of the numerical eigenvalues for all solution modes, shown along the primary mode's eigencurve, for a full upwind DG discretization with $P = 8$ and $\bar{k} = \pi/6 \approx 0.52$.

We now show that the well-resolved part of the solution within Ω_e at time t will match the well-resolved part of the solution within Ω_{e+1} at time $t + \tau_h$, where $\tau_h = h/a$. From Eqs. (24–26), one has that the well-resolved part of the solution, u^W, is given by

$$u^W_{e+1}(\xi, t + \tau_h) = \sum_{m \in \mathbb{W}} A_m \, \sigma_m(\xi) \, \exp[i(k x_{e+1} - w_m t)] \exp(-i w_m \tau_h) \, , \tag{30}$$

and since $w_m = a k^*_m$ and $\tau_h = h/a$, one has through Eq. (29) that

$$\exp(-i w_m \tau_h) = \exp(-i k^*_m h) = \exp(-ikh) \exp(-2\pi i q_m) = \exp(-ikh) \, , \tag{31}$$

provided that $q_m \in \mathbb{Z}$, and therefore

$$u^W_{e+1}(\xi, t + \tau_h) = \sum_{m \in \mathbb{W}} A_m \, \sigma_m(\xi) \, \exp[i(k x_{e+1} - w_m t)] \exp(-ikh) = u^W_e(\xi, t) \, , \tag{32}$$

since by definition $x_{e+1} - x_e = h$.

We conclude that the numerical eigenmodes related to well-resolved wavenumbers, i.e. those within the linear regions of dispersion/diffusion curves, will propagate correctly the components of the numerical solution associated to their wavenumbers. In this sense, all these modes can be considered of physical character. The remaining numerical eigenmodes will be detrimental to the solution accuracy as they introduce significant dispersion and diffusion errors. However, once the apparent wavenumbers remain equispaced along the primary mode's eigencurve as P increases, a larger portion of the numerical modes will contribute to the overall accuracy of the formulation for higher order discretizations, since the (linear) regions of negligible numerical error become larger for higher values of P.

3.3. Effective resolution according to the "1% rule"

All the information regarding dispersion and diffusion characteristics of a DG simulation (of linear advection) is contained in the eigencurves of the primary mode. Therefore, one can anticipate using these eigencurves to quantify the effective resolution that a given hp setting can provide. Here, this resolution is measured in terms of the largest wavenumber that can be accurately resolved to within a tolerance of 1%. We acknowledge that points per wavelength estimates have already been obtained for DG (e.g. [28]), but a more physical interpretation is here explored for our adopted error tolerance.

As shown in Sec. 3.2, the range of wavenumbers for which wave propagation can be considered accurate corresponds to the linear regions of dispersion/diffusion curves. And since diffusion errors have been verified to be more significant than dispersion errors [23, 27], we now focus on defining the extent of the plateau region of diffusion

curves. To that end, it is useful to consider the physical meaning of the imaginary part of $\overline{k^*} = k^* h/(P+1)$. When expressing the modified wavenumber in the form $k^* = k_R^* + ik_I^*$, a propagating wave can be represented as

$$u \propto \exp[i(kx - w^* t)] = \exp(ak_I^* t)\, \exp[i(kx - ak_R^* t)]\,, \tag{33}$$

where the relation $w^* = ak^*$ has been used, so that regarding the wave's amplitude one has

$$|u| \propto \exp(ak_I^* t) = \exp\left(\overline{k_I^*}\, t/\overline{\Delta t}\right), \tag{34}$$

in which $\overline{\Delta t} = \overline{h}/a$ and $\overline{h} = h/(P+1)$. Since $\overline{h}$ is the length measure of one degree of freedom in an hp setting, $\overline{\Delta t}$ is the time it takes for a signal to cross a single DOF. Hence, according to Eq. (34), for each $\Delta t = \overline{\Delta t}$, the magnitude of the propagating wave is multiplied by $\exp(\overline{k_I^*})$, which can then be regarded as a *damping factor per DOF*.

In particular, for a damping factor of 99%, the value of $\overline{k_I^*}$ would be $\ln(0.99) \approx -0.01$. As we shall subsequently demonstrate, this value appears to be a good choice to define the border of the plateau region for each polynomial order. The "1% rule" then consists in relying on the wavenumber $k = k_{1\%}$ for which $\exp(\overline{k_I^*}) = 0.99$ to differentiate between regions of negligible ($k < k_{1\%}$) and significant ($k > k_{1\%}$) dissipation.

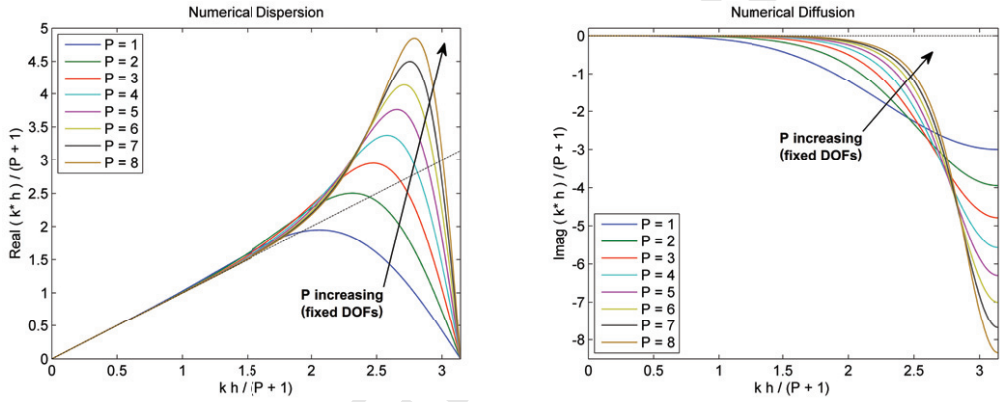

Figure 4: Dispersion (left) and diffusion (right) eigencurves of the full upwind DG formulation for increasing polynomial order P. Note that only positive wavenumbers are shown. The dotted lines represent the exact linear advection behaviour.

Fig. 4 shows the variation of dispersion and diffusion characteristics with the polynomial order P for the full upwind DG scheme. Particularly, the plateau region in the diffusion curves becomes larger for increasing orders. Given P, it is possible to determine the largest value of $\overline{k}_{1\%}$ within the plateau region through the 1% rule. Then, given h, one can obtain the corresponding value of $k_{1\%}$. Fig. 4 also shows that the dissipation affecting wavenumbers outside the plateau region increases with P. A summary of the relevant quantities obtained from the diffusion curves is provided in Table 1 for $P = 1, \ldots, 8$.

Table 1: Relevant diffusion-based quantities of full upwind DG for increasing P

P	$\lvert\overline{k}\rvert_{1\%}$	$\lvert kh\rvert_{1\%}$	DOFpW	$(\overline{k_I^*})_\pi$	$\exp(\overline{k_I^*})_\pi$
1	0.5635	1.127	11.15	−3.00	4.98×10^{-2}
2	0.8721	2.616	7.20	−3.95	1.93×10^{-2}
3	1.0825	4.330	5.80	−4.79	8.31×10^{-3}
4	1.2327	6.164	5.10	−5.57	3.81×10^{-3}
5	1.3451	8.071	4.67	−6.32	1.80×10^{-3}
6	1.4324	10.027	4.39	−7.01	9.03×10^{-4}
7	1.5022	12.018	4.18	−7.60	5.00×10^{-4}
8	1.5594	14.035	4.03	−8.34	2.39×10^{-4}

The second and third columns in Table 1 show the values of $|\overline{k}|_{1\%}$ and $|kh|_{1\%}$, respectively, that can be achieved within an *hp* setting with full upwind DG. Through these values, one can also estimate the coarsest mesh spacing that can be used in order to resolve scales up to a given wavenumber. The fourth column contains the associated number of degrees of freedom per wavelength, DOFpW $= 2\pi/\overline{k}_{1\%}$. This column shows that the DG discretization becomes more efficient *per degree of freedom* as the polynomial order is increased. In fact, spectral-like resolution [30] is approached for increasing P on a per degree of freedom basis, as shown in Fig. 4.

Finally, the last two columns in Table 1 show respectively the values of $\overline{k_I^*}$ at $\overline{k} = \pi$ and the associated damping factors per DOF, $\exp(\overline{k_I^*})_\pi$. These quantities represent the amount of dissipation affecting the smallest captured scales and can be seen to become stronger for increasing P. For $P = 2$, where $\exp(\overline{k_I^*})_\pi \approx 2\times10^{-2}$, the smallest scales would propagate more than two DOFs to suffer the same damping provided for a single DOF by the $P = 7$ discretization, in which $\exp(\overline{k_I^*})_\pi \approx 5\times10^{-4}$. This is probably an extra advantage of employing higher order discretizations, since as previously recognised a faster damping of the poorly-resolved scales further precludes them from polluting the numerical solution.

4. Experiments in Burgers turbulence

In order to assess the methodology proposed in Sec. 3.3 for non-linear problems, the forced Burgers turbulence [31] problem was considered. Our forcing approach follows that of [32], where a white-in-time random force $F(x,t)$ is employed with Fourier components

$$F_k(t) = \frac{A\,\sigma_k(t)}{\sqrt{\Delta t}\,\sqrt{k}}\,, \quad \text{for } k = \frac{2\pi n}{L} \text{ and } n \in \mathbb{Z}\,, \tag{35}$$

where k stands for the wavenumber, A is an amplitude constant, σ_k is a standard Gaussian random function (white-in-time), while Δt and L are the time step and the length of the domain used in the simulation. This particular type of forcing has been adopted in previous studies [33, 34] because it yields a $-5/3$ slope for the inertial range of the energy spectrum and is therefore more representative of Navier-Stokes turbulence. In what follows, this forcing approach is applied to the inviscid Burgers equation.

The forcing cut-off wavenumber k_c is normally chosen to be inside the dissipation range, but here we restrict the effect of the forcing term to the inertial range so that it would not counteract the diffusion provided by the DG scheme on the (numerically induced) dissipation range. We note however that once the statistically steady state is achieved, the energy transfer throughout the cascade mechanism is defined by the larger (forced) scales and thus remains constant across the unforced inertial range. The considered Burgers equation with added forcing takes the form

$$\frac{\partial u}{\partial t} + \frac{1}{2}\frac{\partial u^2}{\partial x} = \frac{A_F}{\sqrt{\Delta t}} \sum_{N\in\mathbb{N}_F} \frac{\sigma_N(t)}{\sqrt{|N|}} \exp\left(i\,\frac{2\pi N}{L}x\right), \tag{36}$$

where $\mathbb{N}_F = \{\pm1, \ldots, \pm N_c\}$ and the cut-off wavenumber is $k_c = 2\pi N_c/L$, i.e. $F_k = 0$ if $k > k_c$. The Gaussian variable σ_N is generated from a standard distribution (zero mean and unit variance) for each wavenumber at each new time step.

The full upwind DG scheme was used for the simulations and exact integrations were employed to avoid aliasing errors. For the non-linear term, Gauss-Legendre quadratures were used with the required number of nodes to ensure exact integration. For the forcing term, Galerkin projections of the Fourier components were carried analytically through the relations given in Eqs. (15–17). These projections were however numerically stripped from the secondary modes originating from each single Fourier component by means of a 'filtering' procedure based on the system of eigenmodes discussed in Sec. 3.1. A detailed description of this procedure is provided in the Appendix.

The test cases addressed here are summarized in Table 2, where letters (a, b, c) refer to the total number of DOFs while numbers $(1, \ldots, 7)$ refer to the polynomial order employed in each case. The number of mesh elements can be evaluated as $N_{\text{dof}}/(P+1)$. For all the cases, Eq. (36) was solved within $\Omega = [-1, 1]$ (and so $L = 2$) with periodic boundary conditions and started from a constant initial condition $u_0 = 1$. Time-stepping was carried with an explicit third-order Runge-Kutta TVD algorithm [35] with $\Delta t = 4\times10^{-5}$ in all test cases, yielding $CFL \approx 0.1$ for the stiffest case ($c7$).

Table 2: Summary of test cases (and their shorthand acronyms)

$N_{dof}\backslash P$	1	2	3	4	5	6	7
1024	$a1$	$a2$	$a3$	$a4$	$a5$	$a6$	$a7$
2048	$b1$	$b2$	$b3$	$b4$	$b5$	$b6$	$b7$
4096	$c1$	$c2$	$c3$	$c4$	$c5$	$c6$	$c7$

The forcing amplitude constant was set to $A_F = 1/2$ for all test cases. Time integrations were performed over the interval $0 \leq t \leq 600$. A snapshot of the solution at $t = 600$ for the case $c7$ is shown in Fig. 5 along with the history of the space-averaged fluctuation $u'_{rms}(t)$. For all test cases addressed, a statistical steady state with an ensemble average of $< u'_{rms} > \approx 0.03$ is reached after approximately $t = 50$. The turnover time of the largest eddies can be estimated as $\tau_0 = L/u'_{rms} \approx 67$.

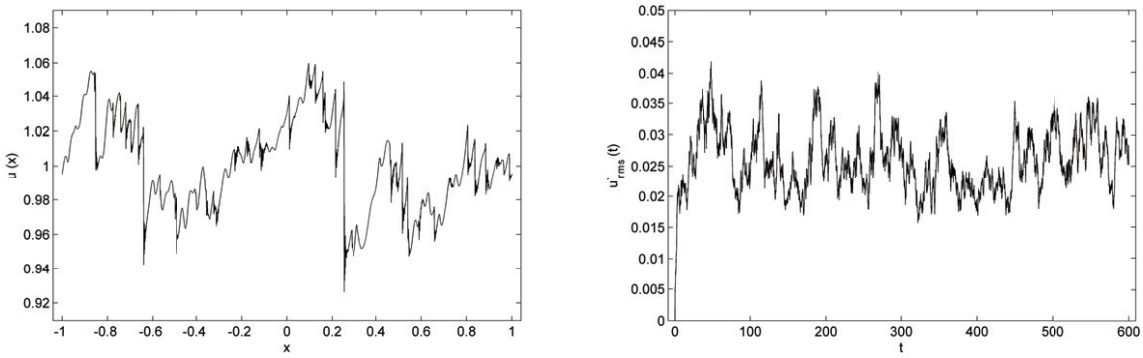

Figure 5: Solution snapshot at $t = 600$ (left) and space-averaged fluctuation $u'_{rms}(t)$ history (right), for the test case $c7$.

The time-averaged energy spectrum $ES(k)$ representing the distribution of turbulent kinetic energy in wavenumber space is given in Fig. 6 again for the case $c7$. This spectrum corresponds to the average of two hundred spectra obtained from successive applications of Taylor's hypothesis [36, 37] over the interval $200 \leq t \leq 600$. Each of these spectra was evaluated by probing of the solution at $x = 0$ over time windows of $\delta t = L/u_0 = 2$. We remark that $u_0 = 1$ remains the average of u within Ω for all times since neither the forcing nor the non-linear dynamics of the Burgers equation affect the average value (component $k = 0$) of the solution.

For all cases addressed, the forcing in Eq. (36) was implemented with $N_c = 80$. As a result, the energy spectrum shown in Fig. 6 features the $-5/3 \approx -1.7$ slope up to $\log_{10}(k_c) = \log_{10}(\pi N_c) \approx 2.4$, as expected of the forcing strategy adopted. After that, a slope of -2, typical of unforced Burgers turbulence [31], takes place until numerical diffusion is seen to affect the spectrum. The effective hp resolution estimated by the 1% rule for this case is shown as a vertical line in Fig. 6. The estimate accurately pinpoints the beginning of the dissipation range. Another effect of the numerical errors is seen in the form of a hump on the energy spectrum near the wavenumber given by the 1% rule ($k_{1\%}$). This hump becomes more noticeable and concentrated for higher values of P, and is possibly connected to dispersion errors, as discussed later. The accuracy of the 1% rule's estimates is very good for all the cases addressed and are even better for the higher orders, where the impact of numerical errors is more localized (in wavenumber space).

The effect of mesh refinement is shown in Fig. 7, where the energy spectra of cases $a4$, $b4$ and $c4$ are depicted. Once again, the vertical lines mark the values of $k_{1\%}$ obtained from the 1% rule and these match quite well the beginning of the dissipation range for each test case. Fig. 7 also helps to clarify *why* the DG formulation can be suitable for under-resolved simulations of turbulence: the numerical discretization is capable of resolving scales up to $k_{1\%}$ with good accuracy while dissipation is provided at the end of the energy spectrum in the form of numerical diffusion. In this sense, the DG-uDNS approach seems closer to hyper-viscosity approaches than to LES approaches based on (explicit or implicit) subgrid-scale modelling.

In the application of the 1% rule, although $|kh|_{1\%}$ varies with P (Table 1), the resolution gain (in log scale) obtained

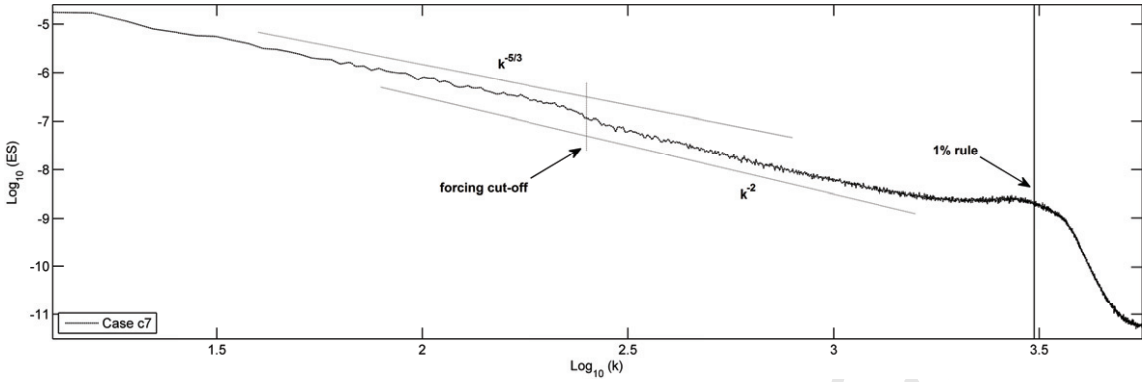

Figure 6: Time-averaged energy spectrum for the test case $c7$, featuring slopes of $-5/3$ and -2 respectively on the forced and unforced regions of the inertial range, as well as a numerical dissipation region taking place as predicted by the 1% rule (vertical line).

with a given mesh refinement factor $f = h/h'$ does not depend on P. This is because, for each P,

$$\log(k'_{1\%}) - \log(k_{1\%}) = \log\left(\frac{|kh|_{1\%}}{h'}\right) - \log\left(\frac{|kh|_{1\%}}{h}\right) = \log(h/h') = \log(f)\ . \tag{37}$$

In the test cases considered here, where a mesh refinement factor of $f = 2$ separates cases *a*-*b* or *b*-*c* for each value of P, the expected resolution gain is given by $\log_{10}(2) \approx 0.3$ which is also visible in Fig. 7.

On the other hand, the actual value of $k_{1\%}$ is strongly dependent on P. The effect of increasing P is considered in Fig. 8, where compensated spectra (for the unforced inertial range) are shown for cases $c1, c2, \ldots, c7$. The horizontal lines correspond exactly to the same value of -2.23, which was defined so as to fit the compensated unforced inertial range of test case $c7$. This value is taken as a reference for all the inertial ranges shown in Fig. 8. The estimates for the beginning of the dissipation range obtained from the 1% rule are again depicted as vertical lines at the right end of each horizontal line. The energy spectra in question correspond to a fixed number of DOFs and, as P increases in Fig. 8, mesh spacing therefore becomes coarser. The vertical lines corresponding to the 1% rule highlight that, for a given number of DOFs, employing higher-order discretizations along with coarser meshes yields superior resolution but, as predicted in Table 1, the gain in resolution obtained by increasing P (with fixed DOFs) is not very significant when the polynomial order is already very large (say, $P > 5$).

Another feature seen in Fig. 8 are the humps on each energy spectrum near their respective values of $k_{1\%}$, which become more concentrated (taller and narrower) as P increases. An explanation for the origin of the humps was first suggested as follows. From the dispersion eigencurves in Fig. 4, one can differentiate two portions of wavenumbers within the poorly-resolved region (between $\overline{k}_{1\%}$ and π). The first portion has wavenumbers which propagate faster than they should, while the second portion contains wavenumbers propagating slower than they should (when compared to the exact behaviour). The intersection of line $\overline{k^*} = \overline{k}$ with the dispersion eigencurves (after their maxima) separates these two portions. Since the considered energy spectra were obtained through the application of Taylor's hypothesis, the energy of the first/second portion could have been attributed to wavenumbers much bigger/smaller than $k_{1\%}$. As a result, dispersion errors related to the first/second portion would be responsible for an accumulation of energy after/before $k_{1\%}$. Further, as the poorly-resolved region becomes narrower and subjected to a stronger dissipation with increasing P, so the associated hump would become more concentrated. Case $P = 1$ is peculiar because dispersion errors are only significant for the second wavenumbers' portion, by which energy should accumulate almost exclusively before $k_{1\%}$. This is indeed observed in Fig. 8, where the energy spectrum of test case $c1$ is seen to have an excess of energy along the whole (unforced) inertial range.

Although plausible and consistent with the energy spectra obtained, the interpretation provided above is not conclusive in demonstrating that the observed humps are just an artefact from Taylor's hypothesis. To further investigate the issue, some energy spectra were evaluated directly in space (at a given time) through a discrete Fourier transform based on equispaced points, however avoiding element interfaces. These energy spectra (not shown) were found to be highly oscillatory at the poorly-resolved scales ($k > k_{1\%}$), yet humps similar to those shown in Fig. 8 could clearly

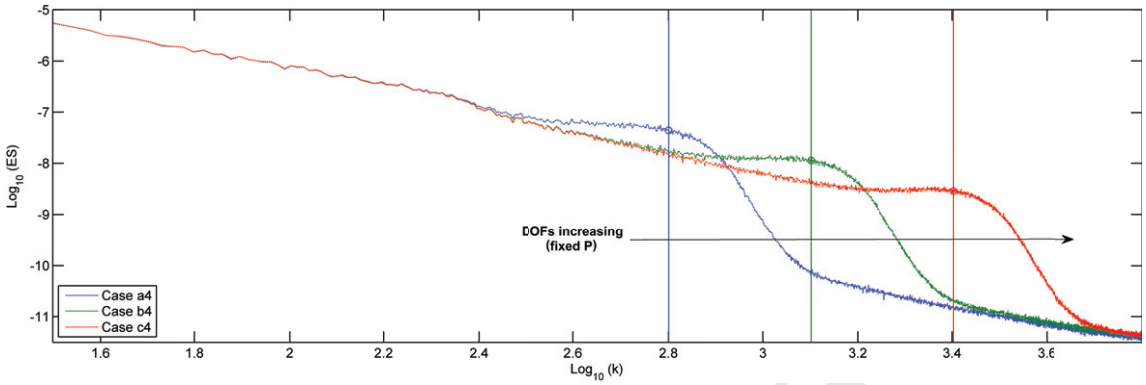

Figure 7: Energy spectra of the $P = 4$ test cases ($a4$, $b4$, $c4$) along with the 1% rule estimates for the beginning of the dissipation range (vertical lines). Circles are used pinpoint the intersection between the energy spectra and their respective 1% rule estimates.

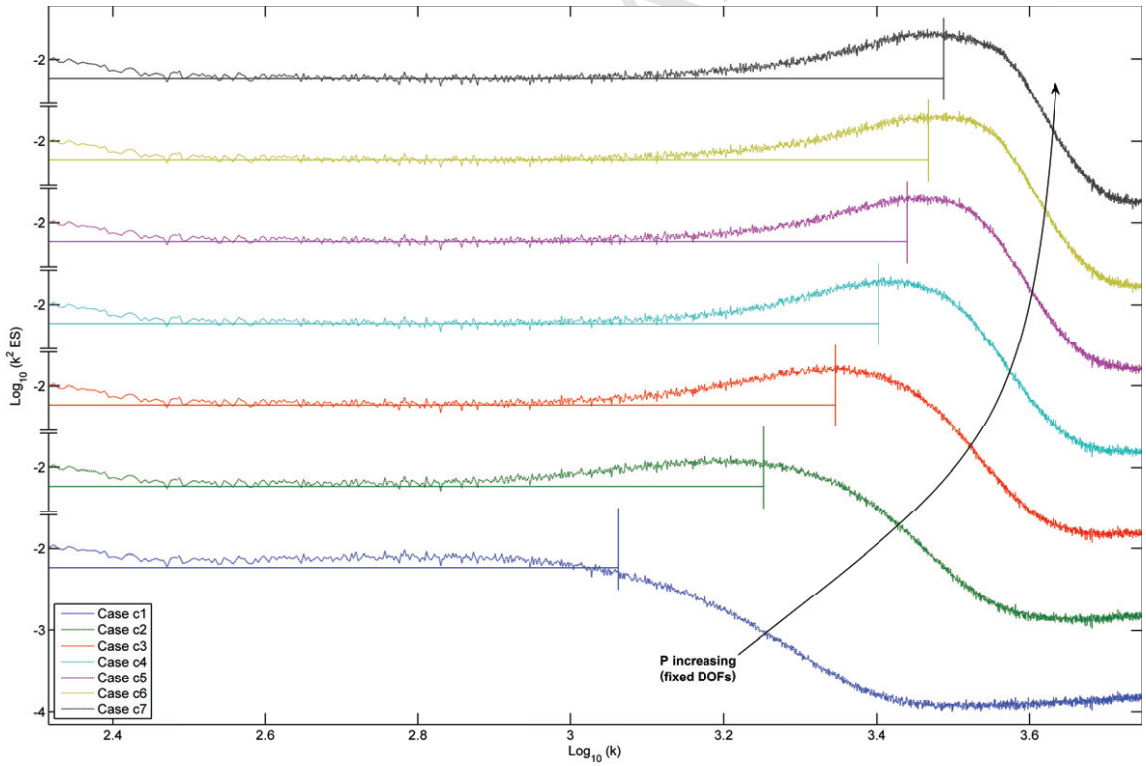

Figure 8: Compensated spectra (for the unforced inertial range) of test cases $c1, c2, \ldots, c7$ alongside their respective 1% rule estimates for the beginning of the dissipation range (vertical lines). All horizontal lines correspond to the value -2.23, defined to fit the inertial range of test case $c7$.

be distinguished in the vicinity of $k_{1\%}$. This highly oscillatory behaviour is believed to be associated with the strong interface discontinuities induced by the shocks which are peculiar to Burgers turbulence. Such results seem to indicate that these humps are not an artefact from Taylor's hypothesis as induced by dispersion errors. Additional investigation is however required to better understand their primary cause.

In any event, the 1% rule proved to be, even in a non-linear setting, reliable in predicting the wavenumber $k_{1\%}$ where numerical errors become significant and after which a numerically induced dissipation range takes place. It provides guidelines for designing an hp approximation space thus clarifying *how* the DG formulation can be better used for under-resolved turbulence simulations. In particular, the use of higher-order discretizations along with coarser meshes is expected to be the most efficient way to translate available resources into resolution power. A comparison between test cases $a1$ and $a7$, which have the same number of DOFs, is shown in Fig. 9 for $t = 600$. The case with a $(7 + 1)/(1 + 1) = 4$ times coarser mesh but $P = 7$ can capture a much broader range of small structures. This feature has also been recognized in previous works [17, 18]. We stress that P-type refinement has long been recognized as more efficient than h-type refinement [4, 25] owing to the exponential (also called spectral) convergence property, but this only holds for well-resolved simulations, where all the wavenumbers captured are well within the linear regions of dispersion and diffusion curves, see [27]. Here we highlight the advantages of favouring P over h in under-resolved turbulence simulations.

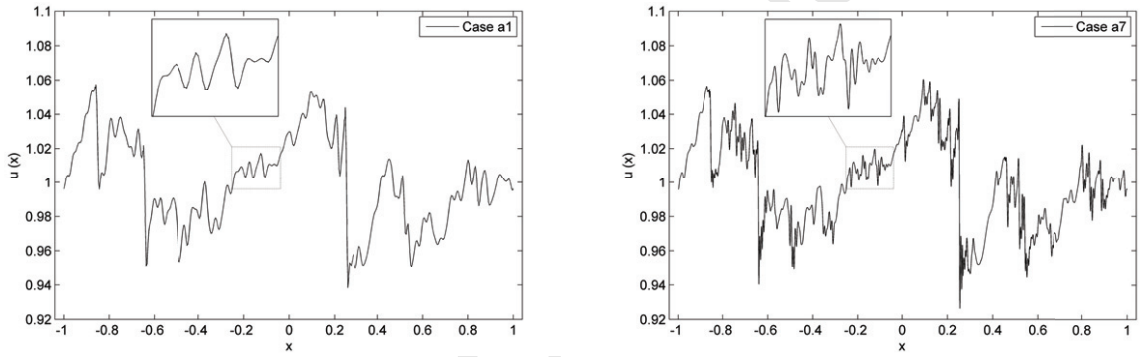

Figure 9: Comparison between solution snapshots at $t = 600$ for test cases $a1$ (left) and $a7$ (right). Though having the same number of DOFs, the higher-order simulation is able to capture a much broader range of small structures.

The comparison in Fig. 9 is appropriate because the random number generator employed for the forcing variable $\sigma_k(t)$ is deterministic and therefore the same forcing function was used in both test cases through the whole integration period. We note however that the computational cost of spectral/hp methods in terms of floating point operations clearly does not linearly scale with DOFs. Nevertheless, on emerging hardware, large scale computations required for turbulence simulations at high Reynolds number are becoming more communication bandwidth-limited than floating point operation-limited and therefore the total number of DOFs is becoming a more relevant measure of performance.

5. Concluding remarks

A linear dispersion-diffusion analysis was employed to provide direct guidelines for the selection of spatial resolution in simulation of turbulence through the under-resolved DNS (uDNS) approach via high-order discontinuous Galerkin (DG) spectral/hp methods. The role of secondary numerical modes, peculiar to spectral/hp methods, was discussed and clarified. It was shown that the secondary modes replicate the behaviour of the primary ones so that essentially all of DG's propagation properties (for linear advection) are given in the dispersion/diffusion eigencurves of the primary modes. From these curves, numerical errors were assessed (diffusion in particular) and their effect on poorly-resolved scales was quantified. A simple criterion named "1% rule" was then proposed to estimate the effective resolution provided by an hp setting in terms of the largest wavenumber $k_{1\%}$ that can be accurately resolved by the approximation space.

Though strictly valid for linear advection, the 1% rule was tested against Burgers turbulence and found to predict quite accurately the beginning of the (numerically induced) dissipation range on the energy spectra of under-resolved

simulations. The results shed some light on *why* the DG formulation might be able to provide good results for uDNS without sub-grid scale models. Essentially, the numerical discretization is capable of resolving scales up to $k_{1\%}$ with high accuracy while providing dissipation at the end of the energy spectrum in the form of numerical diffusion. In this sense, the DG-uDNS approach seems closer to hyper-viscosity approaches than to LES (or iLES) approaches based on explicit (or implicit) SGS modelling. In addition, the 1% rule can provide useful guidelines on *how* to better use DG for uDNS. In particular it was shown that, given a limited number of degrees of freedom, the use of higher-order polynomials along with coarser meshes is the best way to translated available resources into resolution power. The advantages of this strategy (as compared to mesh refinement) were first pointed out in [18], but on a more qualitative basis.

We stress that the 1% rule is not expected to be directly applicable (in its present form) to all kinds of turbulence problems, including Navier-Stokes turbulence. And it does not indicate whether DG-based under-resolved simulations might diverge numerically due to insufficient resolution. Nevertheless, should the proposed methodology (with due adaptations) be valid for real turbulent flows, the concept of effective resolution (embodied in $k_{1\%}$) would play in the uDNS context the role played by the filter width in classic LES. While an SGS model in LES (ideally) begins to act on scales smaller than the filter width, in uDNS a strong numerical dissipation provides a sink for the energy cascade at wavenumbers greater than $k_{1\%}$. For the discretization of the Navier-Stokes equations in three dimensions, the smallest captured scales should be affected, amongst other factors, by the numerical (inviscid and viscous) fluxes employed, the mesh topology and type of elements used. Subsequent studies on the applicability of the 1% rule for real three-dimensional turbulent flows are planned for the near future.

Acknowledgements

RCM would like to acknowledge funding under the Brazilian Science without Borders scheme. SJS would like to acknowledge support as Royal Academy of Engineering Research Chair.

Appendix

This section is devoted to the description of how the source term in Eq. (36) was taken into account in the discretization of the forced Burgers turbulence problem considered in Sec. 4.

We start with Eq. (36) written in the form

$$\frac{\partial u}{\partial t} + \frac{\partial f}{\partial x} = S \ , \tag{38}$$

where $f = u^2/2$ and the source term is given by

$$S = \frac{A_F}{\sqrt{\Delta t}} \sum_{N \in \mathbb{N}_F} \frac{\sigma_N(t)}{\sqrt{|N|}} \exp\left(i k_N x\right) , \tag{39}$$

in which $k_N = 2\pi N/L$. The reader is referred to Sec. 4 for the definition of the remaining variables.

After the customary steps, recall Sec. 2, the semi-discrete equation for the evolution of the element-wise coefficients of Ω_e can be found, namely

$$\frac{h}{2}\frac{\partial c_j}{\partial t} = \int_{\Omega_{st}} f\, \phi_j' \, d\xi \, - \, (\tilde{f}\phi_j)|_{\Omega_e^R} \, + \, (\tilde{f}\phi_j)|_{\Omega_e^L} \, + \, \frac{h}{2}\int_{\Omega_{st}} S\, \phi_j \, d\xi \ , \tag{40}$$

where Ω_e^L and Ω_e^R denote the left and right boundaries of element Ω_e, respectively, and $\tilde{f}$ is the (full upwind) numerical flux evaluated at the respective interfaces. Unpacking the last integral above leads to the term

$$\int_{\Omega_{st}} \exp\left[i k_N \left(x_e + \xi h/2\right)\right] \phi_j(\xi)\, d\xi \, = \, \exp\left(i k_N x_e\right) \int_{\Omega_{st}} \exp\left(i k_N h \xi/2\right) \phi_j(\xi)\, d\xi \, = \, \exp\left(i k_N x_e\right) \alpha_j(k_N h) \ , \tag{41}$$

where x_e denotes the centre of Ω_e and α_j is given analytically in Eqs. (15–17).

In vector form, Eq. (40) is given by

$$\frac{h}{2}\frac{\partial \vec{c}}{\partial t} = \int_{\Omega_{st}} f\,\vec{\phi}'\,d\xi - (\tilde{f}\vec{\phi})|_{\Omega_e^R} + (\tilde{f}\vec{\phi})|_{\Omega_e^L} + \frac{h}{2}\vec{S}_\alpha\,, \tag{42}$$

in which $\vec{c} = \{c_0, \ldots, c_P\}^T$ and

$$\vec{S}_\alpha = \frac{A_F}{\sqrt{\Delta t}} \sum_{N\in\mathbb{N}_F} \frac{\sigma_N(t)}{\sqrt{|N|}} \exp(ik_N x_e)\,\vec{\alpha}(k_N h) \tag{43}$$

where $\vec{\alpha} = \{\alpha_0, \ldots, \alpha_P\}^T$. As discussed in Sec. 3.1, the projection of each single Fourier mode is expected to energize several $(P+1)$ numerical modes with only one of them corresponding to the actual (baseline) wavenumber of the underlying Fourier component. To avoid this, we replace $\vec{S}_\alpha$ by $\vec{S}_\beta$ in Eq. (42), where $\vec{\beta}$ can be regarded as a filtered version of $\vec{\alpha}$ which energizes only the primary eigenmode originating from each Fourier component of the forcing term.

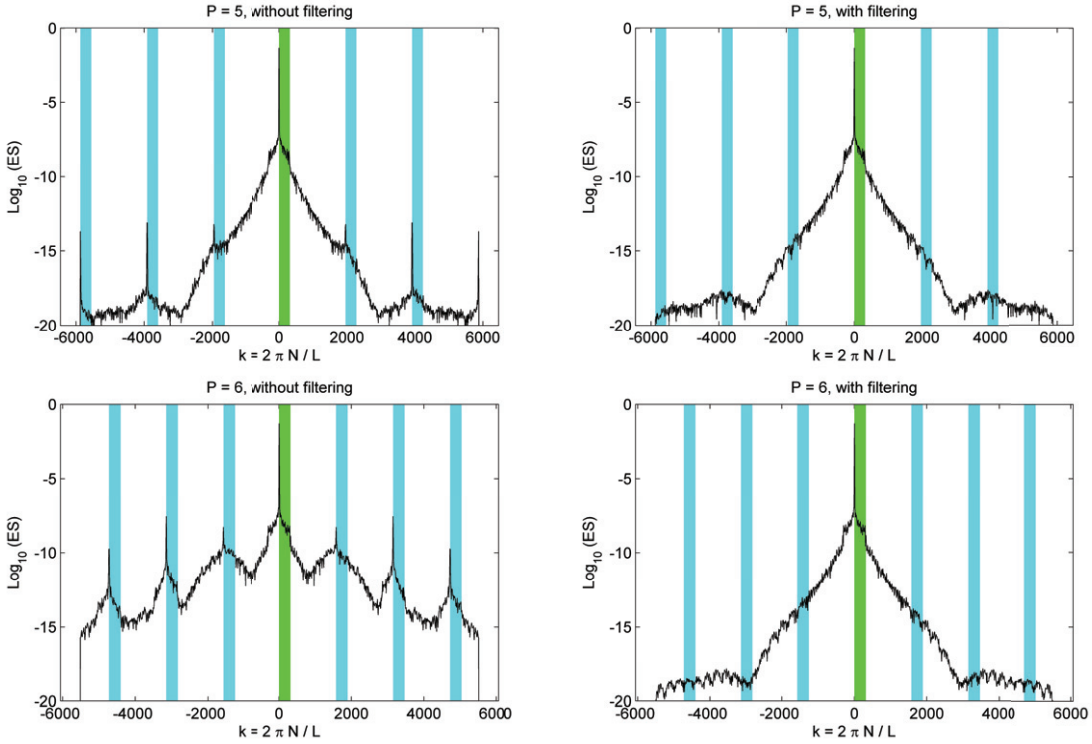

Figure 10: Comparison between unfolded energy spectra of simulations carried without (left) and with (right) filtering, exemplified for $P = 5$ (top) and $P = 6$ (bottom). The highlighted wavenumbers near $k = 0$ correspond to the positive Fourier components of the forcing term. The remaining highlighted wavenumbers are their respective secondary components which can be avoided through the proposed filtering.

From Eqs. (21–23), the amplitude A_m of a numerical eigenmode energized by a given Fourier component can be obtained from the projection array $\vec{\alpha}$ of such Fourier mode through the relation $\vec{A} = \boldsymbol{\mathcal{V}}^{-1}\vec{\alpha}$, where $\vec{A} = \{A_0, \ldots, A_P\}^T$ and $\boldsymbol{\mathcal{V}} = \{\vec{v}_0, \ldots, \vec{v}_P\}$ is the matrix whose columns are the eigenvectors related to the projection operator as defined in Eqs. (19–20). Let M be the index of the primary eigenmode according to the sorting adopted for the entries of $\vec{A}$. We seek $\vec{\beta}$ such that $\vec{B} = \boldsymbol{\mathcal{V}}^{-1}\vec{\beta}$ with $\vec{B} = \{0, \ldots, 0, A_M, 0, \ldots, 0\}^T$, which can be expressed as $\vec{B} = \boldsymbol{\mathcal{F}}_M\vec{A}$, where $\boldsymbol{\mathcal{F}}_M$ is employed to filter out from $\vec{A}$ all the secondary eigenmodes and retain only the primary one (of index M). Hence, $(\boldsymbol{\mathcal{F}}_M)_{i,j} = \delta_{i,M}\,\delta_{M,j}$ in which $\delta_{i,j}$ is the Kronecker delta. The resulting expression for $\vec{\beta}$ is

$$\vec{\beta} = \boldsymbol{\mathcal{V}}\vec{B} = \boldsymbol{\mathcal{V}}\boldsymbol{\mathcal{F}}_M\vec{A} = \boldsymbol{\mathcal{V}}\boldsymbol{\mathcal{F}}_M\boldsymbol{\mathcal{V}}^{-1}\vec{\alpha}\,. \tag{44}$$

We note that index M can be identified from the one-to-one correspondence between eigenvalues and eigenvectors in Eqs. (19-20), since a primary eigenvalue can be more easily distinguished from the secondary ones when compared along dispersion-diffusion curves.

To illustrate the proposed filtering technique, we consider two test cases for $P = 5$ and $P = 6$, with and without filtering. Simulations carried without filtering led to early numerical divergence, especially for the highest polynomial orders. To obtain some results before divergence, simulations were integrated in time until $t = 1$ and compared. The energy spectra evaluated through a discrete Fourier transform (in space) are given in Fig. 10. Note that "unfolded" energy spectra are considered in Fig. 10, where positive and negative wavenumbers are distinguished. Symmetrical plots are obtained due to the conjugate symmetry of the forcing term, which is required to guarantee a real solution at all times. The highlighted wavenumbers near $k = 0$ correspond to the positive Fourier components of the forcing term. The remaining highlighted wavenumbers are their respective secondary components (recall Fig. 3) which can be avoided through the proposed filtering. If these secondary components are not avoided, they will grow in time and eventually lead to numerical divergence. Note that non-linear interactions rapidly energize wavenumbers in between the highlighted ranges.

References

[1] F. Grinstein, L. Margolin, W. Rider, Implicit large eddy simulation: computing turbulent fluid dynamics, Cambridge University Press, 2007.
[2] S. Pope, Ten questions concerning the large-eddy simulation of turbulent flows, New Journal of Physics 6 (1) (2004) 35.
[3] P. Spalart, Strategies for turbulence modelling and simulations, International Journal of Heat and Fluid Flow 21 (3) (2000) 252–263.
[4] G. Karniadakis, S. Sherwin, Spectral/hp element methods for computational fluid dynamics, 2nd Edition, Oxford University Press, 2005.
[5] G. Karamanos, G. Karniadakis, A spectral vanishing viscosity method for large-eddy simulations, Journal of Computational Physics 163 (1) (2000) 22–50.
[6] R. Kirby, G. Karniadakis, De-aliasing on non-uniform grids: algorithms and applications, Journal of Computational Physics 191 (1) (2003) 249–264.
[7] A. Uranga, P. Persson, M. Drela, J. Peraire, Implicit large eddy simulation of transition to turbulence at low Reynolds numbers using a discontinuous Galerkin method, International Journal for Numerical Methods in Engineering 87 (1-5) (2011) 232–261.
[8] A. Beck, T. Bolemann, D. Flad, H. Frank, G. Gassner, F. Hindenlang, C. Munz, High-order discontinuous Galerkin spectral element methods for transitional and turbulent flow simulations, International Journal for Numerical Methods in Fluids 76 (8) (2014) 522–548.
[9] C. Liang, S. Premasuthan, A. Jameson, Z. Wang, Large eddy simulation of compressible turbulent channel flow with spectral difference method, in: Proceedings of the 47th AIAA Aerospace Sciences Meeting (AIAA Paper 2009-402), Orlando, USA, 2009.
[10] M. Parsani, G. Ghorbaniasl, C. Lacor, E. Turkel, An implicit high-order spectral difference approach for large eddy simulation, Journal of Computational Physics 229 (14) (2010) 5373–5393.
[11] B. Vermeire, J. Cagnone, S. Nadarajah, ILES using the correction procedure via reconstruction scheme, in: Proceedings of 51st AIAA Aerospace Sciences Meeting (AIAA Paper 2013-1001), Grapevine, USA, 2013.
[12] B. Vermeire, S. Nadarajah, P. Tucker, Canonical test cases for high-order unstructured implicit large eddy simulation, in: Proceedings of the 52nd AIAA Aerospace Sciences Meeting (AIAA Paper 2014-0935), National Harbour, USA, 2014.
[13] R. Kirby, S. Sherwin, Stabilisation of spectral/hp element methods through spectral vanishing viscosity: application to fluid mechanics modelling, Computer Methods in Applied Mechanics and Engineering 195 (23) (2006) 3128–3144.
[14] S. Collis, Discontinuous Galerkin methods for turbulence simulation, in: Proceedings of the 2002 Center for Turbulence Research Summer Program, 2002, pp. 155–167.
[15] S. Collis, K. Ghayour, Discontinuous Galerkin methods for compressible DNS, in: Proceedings of the 4th ASME/JSME Joint Fluids Summer Engineering Conference, 2003, pp. 1777–1786.
[16] L. Wei, A. Pollard, Direct numerical simulation of compressible turbulent channel flows using the discontinuous Galerkin method, Computers & Fluids 47 (1) (2011) 85–100.
[17] J. Chapelier, M. de la Llave Plata, F. Renac, E. Lamballais, Evaluation of a high-order discontinuous Galerkin method for the DNS of turbulent flows, Computers & Fluids 95 (2014) 210–226.
[18] G. Gassner, A. Beck, On the accuracy of high-order discretizations for underresolved turbulence simulations, Theoretical and Computational Fluid Dynamics 27 (3-4) (2013) 221–237.
[19] G. Taylor, A. Green, Mechanism of the production of small eddies from large ones, Proceedings of the Royal Society of London (A) 158 (895) (1937) 499–521.
[20] C. de Wiart, K. Hillewaert, M. Duponcheel, G. Winckelmans, Assessment of a discontinuous Galerkin method for the simulation of vortical flows at high Reynolds number, International Journal for Numerical Methods in Fluids 74 (7) (2014) 469–493.
[21] L. Margolin, W. Rider, A rationale for implicit turbulence modelling, International Journal for Numerical Methods in Fluids 39 (9) (2002) 821–841.
[22] R. Moura, S. Sherwin, J. Peiró, Modified equation analysis for the discontinuous Galerkin formulation, in: Proceedings of the 10th International Conference on Spectral and High Order Methods (ICOSAHOM), Salt Lake City, USA, 2014.
[23] F. Hu, M. Hussaini, P. Rasetarinera, An analysis of the discontinuous Galerkin method for wave propagation problems, Journal of Computational Physics 151 (2) (1999) 921–946.
[24] F. Hu, H. Atkins, Eigensolution analysis of the discontinuous Galerkin method with nonuniform grids: I. one space dimension, Journal of Computational Physics 182 (2) (2002) 516–545.

[25] J. Hesthaven, T. Warburton, Nodal discontinuous Galerkin methods: algorithms, analysis, and applications, Springer, 2007.
[26] S. Sherwin, Dispersion analysis of the continuous and discontinuous Galerkin formulations, in: B. Cockburn, G. Karniadakis, C. Shu (Eds.), Discontinuous Galerkin Methods: Theory, Computation and Applications, Springer, 2000, pp. 425–431.
[27] M. Ainsworth, Dispersive and dissipative behaviour of high order discontinuous Galerkin finite element methods, Journal of Computational Physics 198 (1) (2004) 106–130.
[28] G. Gassner, D. Kopriva, A comparison of the dispersion and dissipation errors of Gauss and Gauss-Lobatto discontinuous Galerkin spectral element methods, SIAM Journal on Scientific Computing 33 (5) (2011) 2560–2579.
[29] P. Vincent, P. Castonguay, A. Jameson, Insights from von Neumann analysis of high-order flux reconstruction schemes, Journal of Computational Physics 230 (22) (2011) 8134–8154.
[30] S. Lele, Compact finite difference schemes with spectral-like resolution, Journal of Computational Physics 103 (1) (1992) 16–42.
[31] J. Bec, K. Khanin, Burgers turbulence, Physics Reports 447 (1) (2007) 1–66.
[32] A. Chekhlov, V. Yakhot, Kolmogorov turbulence in a random-force-driven Burgers equation, Physical Review E 51 (4) (1995) R2739.
[33] O. Zikanov, A. Thess, R. Grauer, Statistics of turbulence in a generalized random-force-driven burgers equation, Physics of Fluids 9 (5) (1997) 1362–1367.
[34] N. Adams, S. Hickel, S. Franz, Implicit subgrid-scale modeling by adaptive deconvolution, Journal of Computational Physics 200 (2) (2004) 412–431.
[35] S. Gottlieb, C. Shu, Total variation diminishing Runge-Kutta schemes, Mathematics of Computation of the American Mathematical Society 67 (221) (1998) 73–85.
[36] G. Taylor, The spectrum of turbulence, Proceedings of the Royal Society of London. Series A-Mathematical and Physical Sciences 164 (919) (1938) 476–490.
[37] A. Bahraminasab, M. Niry, J. Davoudi, M. Tabar, A. Masoudi, K. Sreenivasan, Taylor's frozen-flow hypothesis in Burgers turbulence, Physical Review E 77 (6) (2008) 065302.